On-Chip Unidirectional Waveguiding for Surface Acoustic Waves along a Defect Line in a Triangular Lattice

Yun Zhou, Naiqing Zhang, Dia’aaldin J. Bisharat, Robert J. Davis, Zichen Zhang, James Friend, Prabhakar R. Bandaru, and Daniel F. Sievenpiper

Phys. Rev. Applied **19**, 024053 — Published 21 February 2023
DOI: 10.1103/PhysRevApplied.19.024053

On-chip unidirectional waveguiding for surface acoustic waves along a defect line in a triangular lattice

Yun Zhou[1,4], Naiqing Zhang[1,4], Dia'aaldin J. Bisharat[2], Robert J. Davis[2], Zichen Zhang[3], James Friend[1], Prabhakar R. Bandaru[1, 2, 3] and Daniel F. Sievenpiper[2, 3]

1 Department of Mechanical Engineering, University of California, San Diego, La Jolla 92093-0411 CA, USA

2 Department of Electrical Engineering, University of California, San Diego, La Jolla, 92093-0411 CA, USA

3 Program in Materials Science, University of California, San Diego, La Jolla 92093-0411 CA, USA

4 These authors contribute equally to the paper.

Email: jfriend@eng.ucsd.edu, pbandaru@eng.ucsd.edu and dsievenpiper@eng.ucsd.edu

The latest advances in topological physics have yielded a toolset for highly robust wave propagation modalities for overcoming obstacles involving beam steering and lateral diffraction in surface acoustic waves (SAWs). However, extant proposals have been limited to the exploitation of spin or valley-polarized phases and rely on non-zero Berry curvature effects. Here we propose and experimentally demonstrate a highly robust guiding principle, which instead employs an intrinsic chirality of phase vortices and maintains a zero Berry curvature for SAWs. Based on a line defect within a true triangular phononic lattice, the guided SAW mode spans a wide bandwidth ($\frac{\Delta\omega}{\omega_{\mathrm{center}}}\sim 10\%$) and is well confined in the lateral direction with 3 dB attenuation within half of a unit-cell. SAW routing around sharp bends with negligible backscatter has been demonstrated. The on-chip integrated design permits unidirectional SAW modes that can enable considerable miniaturization of SAW based devices, with applications ranging from radio frequency devices to quantum information transduction.

I. INTRODUCTION

Surface acoustic waves (SAWs) have been appealing for applications ranging from precise on-chip manipulation of particles and fluids in acoustofluidics [1–10], to probing and controlling elementary excitations in condensed matter [11–16]. In all such applications, low loss SAW guiding is desired. While waveguides [17] are utilized for confinement and control of SAW propagation, beam steering [18] due to anisotropy of the piezoelectric substrate, and lateral diffraction of SAWs cause energy dissipation, degrading the performance. SAW filters are also key components for wireless devices [19,20]. As modern multi-band systems continue to shrink in size, it is becoming increasingly important to miniaturize such SAW components without sacrificing performance. A design scheme to steer the acoustic waves while suppressing backscattering would be of significant benefit.

A promising method to create unidirectional and backscatter-immune SAW waveguides may be through non-reciprocal devices, which are based on a broken time-reversal symmetry (TRS) and can exhibit one-way transmission of propagating waves. For instance, the intrinsic TRS breaking in ferromagnetic materials may lead to non-reciprocal SAW propagation [21–26], due to the different absorption in the $+k$ and $-k$ (k represents the wavenumber) directions. However, the use of magnetic materials in devices is usually undesirable, and manipulation of SAW propagation direction has not been realized in such devices. Another way to achieve acoustic non-reciprocity is to use nonlinear effects [27–30], but the manipulation of propagation direction remains challenging in these nonlinear systems. Topological insulators (TIs) based upon the quantum Hall effect [31,32] has been extended to bosons by introducing external rotational forces for many photonic [33–40] and mechanical/acoustic systems [41–49] to build non-reciprocal waveguides. As such, the realization of non-reciprocal topologically protected modes in the technologically relevant case of SAW has thus far proved elusive. However, true non-reciprocity is not a requirement for suppression of backscatter, and there are innumerable approaches inspired by the quantum spin and valley Hall effects that maintain time-reversal symmetry while demonstrating highly robust transport.

TIs based on quantum spin Hall effect [50–53] yield spin-selective unidirectional passages. Some SAWs like Rayleigh waves show intrinsic spin-momentum locking [97], but it is challenging to excite a mode of a specific spin in such systems. Lattice symmetry breaking can introduce pseudospins by tuning the inter- and intra- cell coupling while maintaining C_{6v} symmetry in honeycomb lattices [54–57], or breaking the z-directional mirror symmetry in bianisotropic materials [58–60], to mimic the quantum spin Hall effect. Unidirectional valley degree of freedom based TI (VTI) waveguides may also be constructed by breaking inversion symmetry in honeycomb lattices [61,62]. These TIs are reciprocal and protected by TRS and still allow for robust and unidirectional wave guiding. We aim to extend related ideas to on-chip phononic devices [63–65]. However, due to the lattice symmetry requirement, most of the existing on-chip designs have utilized suspended structures for bulk acoustic wave or Lamb waves, and an easy corresponding extension for SAWs is still lacking.

Here, we report a scalable, non-suspended, fully integrated, reciprocal, and unidirectional on-chip SAW waveguide fabricated on a lithium niobate ($LiNbO_3$) platform. In our implementation, the unidirectional SAW waveguide is created by a defect boundary in a triangular phononic lattice. We demonstrate that while the triangular lattice has a vanishing Berry curvature, the intrinsic embedded phase vortices give rise to unidirectional wave transport. We prove that, compared to VTIs, our simpler waveguide structures show much better lateral confinement without sacrificing the directionality. The confined, robust, and unidirectional SAW routing phenomenon has been verified through experiments, which demonstrate that our design overcomes the limitation of beam steering in the substrate. The propagating SAW is capable of making sharp turns along the defect-line waveguide (DLW) with low reflection loss.

Previous studies of topological physics in SAW have focused entirely on spin [83] and valley [84] type structures, whereas our DLW employs a different physics, that of rotational symmetry. We reveal the topological origin of the DLW modes by the method of symmetry indicators and show that the edge states are caused by the triangular lattice itself, while spin and valley phases require non-zero Berry curvature. Our device is of practical value, as our structure does not require an expanded supercell for containment (as in spin-like structures) and shows great confinement, thus reducing the bulk size. By incorporating the proposed DLW, there is now a possibility of control and modulation of SAW propagation in any chosen direction over a wide frequency range with a compact device size. Such compact and robust system may benefit many on-chip SAW applications, such as telecommunication, acoustofluidics, bioengineering, as well as in quantum information sciences.

Ⅱ. RESULTS and DISCUSSION

A. Unidirectional SAW waveguide in a triangular lattice with zero Berry curvature

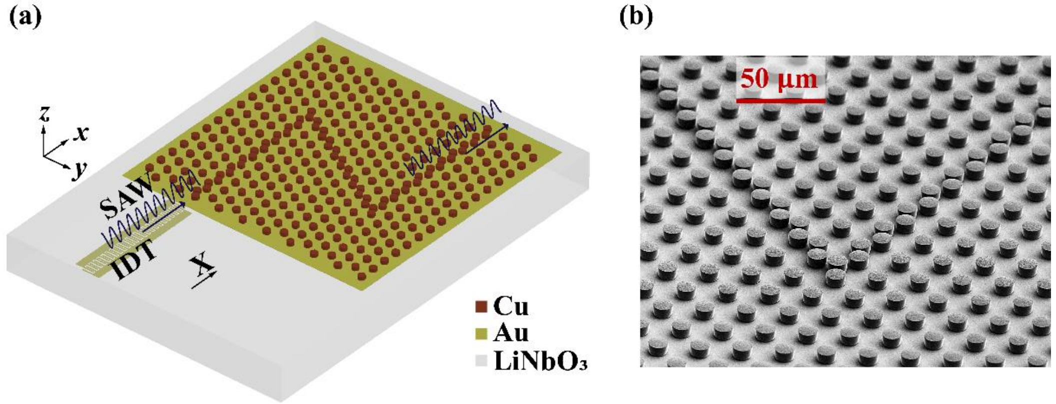

FIG. 1. The DLW for SAW. (a) Schematic of the proposed SAW DLW composed of phononic crystal of copper pillars arranged in a triangular lattice on a 127.68° Y-rotated X-propagating $LiNbO_3$ wafer. The incident SAW in the X direction is provided by a broadband chirped IDT. (b) SEM image with a zoomed-in view of the fabricated SAW waveguide. The Cu pillars are 11.5 µm in diameter and 6.2 µm in height, with lattice constant a=24 µm, grew on a 400 nm Au seed layer on top of a 500 µm $LiNbO_3$ wafer.

The proposed SAW waveguide is formed by a defect line in a triangular array of copper pillars on 127.68° Y-rotated X-propagating $LiNbO_3$ wafer, as shown in **Fig. 1(a)**. The entrance and exit ports of the waveguide are aligned with the X crystal direction of the $LiNbO_3$ wafer. The lattice of identical copper pillars introduces periodic modulation for SAWs, inducing a related dispersion and band structure **[92-96]** (with bands and bandgaps). **Fig. 1(b)** shows a scanning electron microscopy (SEM) image of the fabricated SAW waveguide, where the copper pillars were grown onto the $LiNbO_3$ substrate through electrochemical deposition (see **Appendix A**). To study the SAW propagation, a broadband interdigital transducer (IDT) with a narrow aperture (see **Appendices A** and **B**) is fabricated on the same wafer and excites SAWs in the X direction from the entrance port.

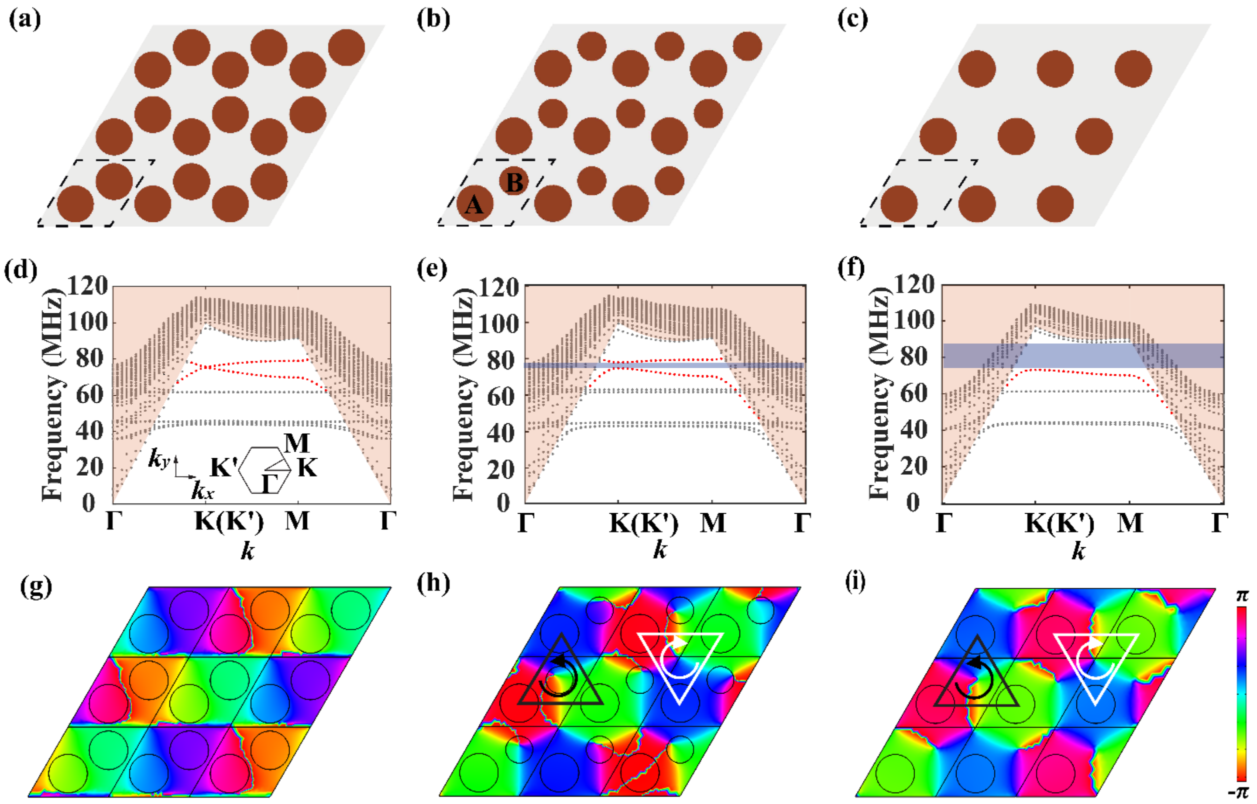

FIG. 2. Phase vortices and intrinsic OAM for a triangular lattice. (a) Honeycomb lattice, (b) VTI with $r_B = 0.8r_A$ and (c) triangular lattice with Cu pillars of 11.5 µm diameter and 6.2 µm height on 500 µm $LiNbO_3$ substrate. Calculated band dispersions along Γ-K (K′)-M-Γ direction for (d) the honeycomb lattice, (e) the VTI, and (f) the triangular lattice. Bandgaps for SAWs due to symmetry breaking are shaded in blue. Bulk acoustic wave bands are shaded in orange. We focus on bands highlighted in red dashed lines this paper. Simulated phase maps for the (g) honeycomb lattice, (h) VTI and (i) the triangular lattice at K. Phase plots for the VTI and the triangular lattice shows two vortices: one at the center of the downward triangles, and one at the center of the upward triangles. The upward triangles Δ and downward triangles ∇ indicate opposite phase vortices.

To understand the characteristics of the proposed SAW waveguide, we study the band dispersion and eigen states of the triangular lattice. It has previously been observed that a Dirac degeneracy for SAW at the K point occurs in a honeycomb lattice consisting of metallic pillars on $LiNbO_3$ [66] (also shown in **Fig. 2(a)** and **(d)**). Through differentiating one pillar from the other in the unit cell by shrinking the diameter of one of the pillars in the honeycomb lattice, say pillar B, as shown in **Fig. 2(b),** the structure may be equated to a SAW VTI [67]. The C_{6v} symmetry of the lattice is reduced to C_{3v}, which lifts the Dirac degeneracy at K and forms a SAW bandgap, as shown in **Fig. 2(e)**. Consequently, topologically protected valley edge states for SAWs are expected to be found in the bandgap formed. Further shrinking the pillar B diameter to zero, the number of copper pillars in the unit cell reduces from two to one, and the honeycomb is transformed into a triangular lattice [68], as shown in **Fig. 2(c)**. Since the SAW modes are supported by the mechanical resonances of the copper pillars [69], reducing the number of pillars by half reduces the number of SAW modes by half. As shown in **Fig. 2(f)**, a larger SAW bandgap then forms from 73.08 MHz to 88.13 MHz. We note here that a previous numerical study in a photonic platform [70] analyzed a similar arrangement, though in their case the physical mechanism naturally differs (mechanical resonances vs electromagnetic modes) and the topological origin of the resulting behavior was not explained, as we will show later.

We observed an intrinsic phase rotation for the out-of-plane displacement u_z in the unit cell of the triangular lattice. The phase distribution map of u_z at the K point of the Brillouin zone for the bands highlighted in red in **Fig. 2 (d), (e) and (f)** for the honeycomb lattice, the valley SAW TI, and triangular lattice are shown in **Fig. 2(g), (h) and (i)**, respectively. These modes are out-of-plane dominant as the in-plane displacement is much smaller compared to the out-of-plane displacement [69]. It may be observed that the phase shows greater uniformity close to the pillars. In the case of the valley SAW TI, **Fig. 2(h)**, the relative position of the pillars leads to two vortices with opposing directions from a 2π phase rotation: one showing a counterclockwise vortex at the center of three pillars arranged in downwards triangles, and one showing a clockwise vortex at the center of three pillars arranged in upward triangles. These phase vortices indicate the presence of circular-polarized orbital angular momentum (OAM) and a chiral property for u_z throughout the bulk of the VTI lattice [71,72]. The OAM waves of opposite signs suggest unidirectional interfacial modes would be supported when the directionality is reinforced rather than opposed at a boundary or interface. Triangular lattice with only one pillar per unit cell may still be mapped to an intrinsic OAM as in a topologically nontrivial VTI, as shown in the phase plot in **Fig. 2(i)**, implying unidirectional confined edge modes would still be supported in the bandgap. However, despite the similarity, the triangular lattice maintains a C_{6v} point group symmetry [100], while the lattice symmetry in a valley structure is reduced to C_{3v}.

The difference in the physical mechanism between the VTI and the triangular lattice can be observed not only from different group symmetries, but also from the Berry curvature. Topological behavior of a VTI is usually described by accumulation of Berry curvature around K (K'), as shown in **Fig. 3(a)**, which is a result of inversion symmetry breaking in the unit cell of VTI (A and B pillars being different). The integral of Berry curvature (Berry phase) around K (K') for a VTI is $\pm\pi$, and this leads to a non-zero valley Chern number of $\pm\frac{1}{2}$ [73]. By contrast, with no TRS breaking or inversion symmetry breaking, the Berry curvature vanishes everywhere in the Brillouin zone for the triangular lattice [69] section 2. As illustrated in **Fig. 3(b)** the Berry curvature is shown to be zero [74,75] around K (K'), in clear contrast to the case of the VTI. This implies that the triangular lattice shows a different topological phase compared to the VTI.

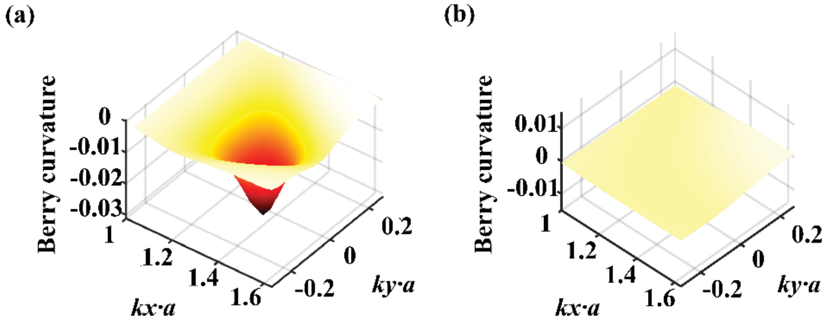

FIG. 3. Berry curvature at K for the VTI and the triangular lattice. Berry curvature for (a) VTI and (b) triangular lattice around K ($\frac{4}{3}\frac{\pi}{a}$, 0). The Berry curvature is zero thoroughout the BZ with no accumulation around K, which shows a clear contrast to that of the VTI.

The spatial arrangement of the phase vortices suggests a gauge dependance on the existence of edge modes along the border. This can be likened to the topological crystalline insulator phases found in Kagome crystals [76–78], where the underlying symmetry is determined by the choice of unit cell. We can imagine the limit of a “breathing” Kagome unit cell as equivalent to a triangular lattice, with each lattice cite partially overlapping with the neighboring cells [78,79]. Unlike Kagome crystals, however, the physical realization given here maintains the C_{6v} rotational symmetry for suitable choices in unit cell. Despite this, it can be seen [69] that for the unit cell definitions that result in C_{3v} edges along finite boundaries (as are studied here) the edge modes can be described by a nontrivial symmetry indicator [80–82] that describes the effect of the phase vortex. The existence of unidirectional modes is therefore a direct consequence of the real space behavior of the finite crystal along certain boundaries, rather than the reciprocal space influence of valley-based effects. The symmetry indicator provides a direct measure of these real space effects, as is visually represented in the phase vortices seen in **Fig. 2(i)**. This verification also provides the underlying mechanism simulated by Yang *et al.* [70] and is covered at length in Davis *et al.* [83]. In the following sections, we demonstrate the existence, confinement, and robustness of the nontrivial interfacial modes in the proposed SAW waveguide in both numerical simulations and experiments.

B. Unidirectional SAW edge states

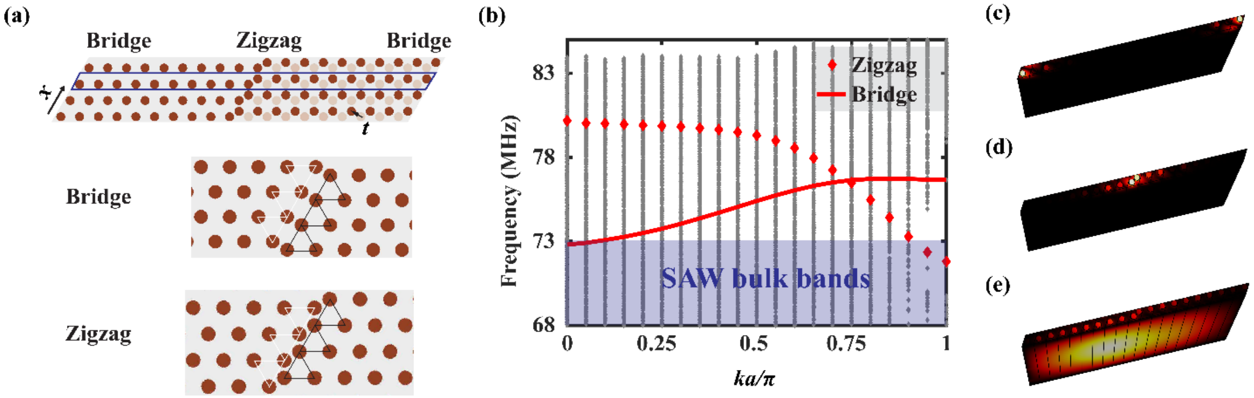

FIG. 4. SAW interfacial modes at the zigzag and the bridge defect lines. (a) (top) A DLW created by shifting one half domain of the triangular phononic crystal of $\vec{t} = \frac{\sqrt{3}}{3}a$ in the direction perpendicular to the waveguide. The light red color shows the positions of the pillars before the shift. A ribbon super cell is highlighted in blue, with a zigzag defect line in the middle and bridge defect line at the edges (as periodic boundary condition is applied in x direction.) (bottom) The bridge defect line and zigzag defect line in the triangular lattice. The upward triangles Δ and downward triangles ∇ indicate opposite phase vortices. (b) Band dispersions for the ribbon super cell. Here the red curves represent edges states at the defect-line boundaries, and the grey dots in the background present bulk acoustic wave modes. (c) Eigen-displacement u_z for the edge mode confined at the bridge defect line, corresponding to the dispersion curve in red solid line. (d) Eigen-displacement u_z for the edge mode confined at the zigzag defect, corresponding to the dispersion curve in red dashed line. (e) Eigen-displacement u_z for the bulk acoustic modes, corresponding to the grey dots in the SAW bandgap.

We first prove, through numerical simulations, the existence of unidirectional SAW edge states, despite zero Berry curvature. We construct a DLW in the lattice where the phase on its two sides shows opposite vortices with enhanced direction of the energy flow at the defect line (see **bottom** figure in **Fig. 4(a)**). Here, a waveguide was created by shifting the right half domain of the triangular lattice $t = \frac{1}{\sqrt{3}}a$ in the direction perpendicular to the zigzag defect line, as illustrated in the **top** figure of **Fig. 4(a)**. It can be observed that the domain on the left of the waveguide is truncated such that the pillars are arranged in downward triangles along the boundary, while along the right side of the waveguide the pillars are arranged in upward triangles. The phase vortices are opposite on the two sides, which leads to energy flux reinforced in one direction, giving rise to unidirectional SAW transport at the defect line.

To find guided modes along the interface, we considered the band dispersion of a ribbon supercell with a zigzag defect line in the middle and a bridge defect line on the edges, as highlighted in the top figure of **Fig. 4(a)**. Periodic boundary conditions are applied in both the x direction and the direction along the waveguide, and the calculated band diagram is plotted in **Fig. 4(b)**. We see new dispersion curves appear in the SAW band gap, that are SAW modes confined at the zigzag and bridge interfaces, as highlighted in red in **Fig. 4(b)**. The zigzag and bridge interfacial modes fall mostly into the SAW bandgap, with their corresponding eigen-displacement (u_z) amplitude fields shown in **Fig. 4(c)** and **Fig. 4(d)**, indicating the existence of the edge states at both the zigzag defect line and the bridge defect line. The edge mode associated to the zigzag defect line (dispersion curve in red dashed line in **Fig. 4(b)**) spans a wider frequency range (71.8 MHz to 80.18 MHz) compared to the edge mode confined at the bridge defect line (72.8 MHz to 76.65 MHz, as shown in dispersion curve in red solid line in **Fig. 4(b)**). Some bulk acoustic wave modes were observed in the SAW bandgap, as shown by the grey dots in the band diagram. These modes decay rapidly into the bulk and do not couple to the SAW modes; therefore, they can be safely ignored. **Fig. 4(e)** shows the u_z of one of the bulk modes and related bulk wave behavior. Since these modes propagate into the bulk at a higher velocity, we expect them to have minor/negligible coupling with our SAW edge modes.

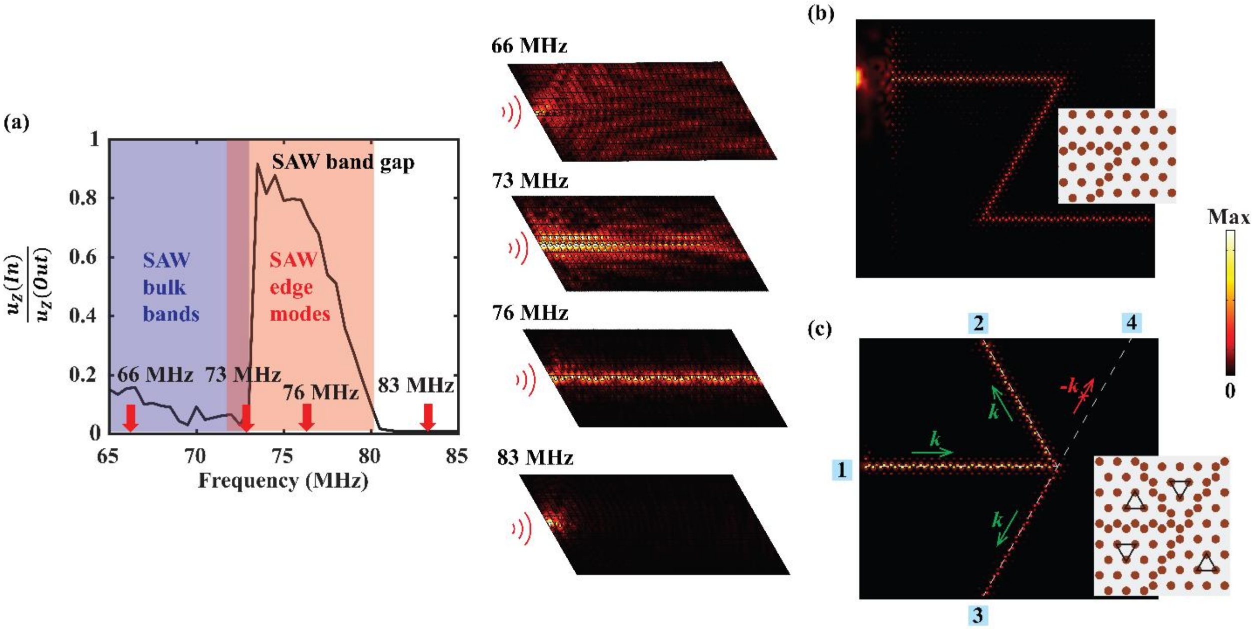

FIG. 5. Unidirectional SAW modes at the DLW. (a) (left) u_z amplitude at the exit port of a straight zigzag DLW of 64a length, normalized by u_z amplitude at the entrance port from 65 MHz to 85 MHz. (right) u_z field plots for the straight zigzag DLW at 66 MHz (within SAW bulk bands), 73 MHz (edge mode within SAW bulk bands), 76 MHz (edge mode within SAW bandgap) and 83 MHz (within SAW bandgap). (b) Simulated u_z field for a Z-shaped zigzag DLW with an excitation of 76 MHz. (c) A "magic T" junction for the zigzag DLW. The "magic T" divide the domain into 4 parts with 60°, 60°, 60°and 180° angles at the junction. The four sub-domains are denoted by the Δ and ∇ respectively. The excitation is at 76 MHz at port 1.

Driven-mode simulations in **Fig.5** prove the existence and unidirectionality of the guided mode. **Fig. 5(a)** shows the u_z amplitude at the exit port of a straight zigzag DLW of 64a length normalized by the u_z at the entrance port. It can be observed that the SAW waveguide has high transmission from 73.08 MHz to 80.18 MHz, related to the edge mode. For frequencies below 73.08 MHz (within the SAW bulk bands), SAWs radiate throughout the whole surface, while for frequencies above 80.18 MHz the bandgap prohibits SAW propagation, leading to low transmission. In **Fig. 5(b),** a zigzag DLW with two 120-degree sharp turns was excited at 76 MHz, demonstrating robust SAW waveguiding with little reflection. To prove the unidirectionality, we simulated a "magic T" junction as shown in **Fig. 5(c)**, constituted from four DLWs that separate the domain into four parts. When sending a wave into port 1, the excited SAW will propagate in the direction in which the wave sees the upward triangles on its left and the downward triangles on its right. As shown in **Fig. 5(c)**, the SAW excited at port 1 couples to port 2 and 3 but not port 4, as the waveguide connected to port 4 only supports SAW in the opposite propagation direction. The triangles, corresponding to the phase vortices, uniquely determine the direction of propagation, unlike ordinary defect modes. Consequently, it has been clearly indicated that edge states at the DLW are unidirectional.

C. Confinement and robustness of the SAW DLW

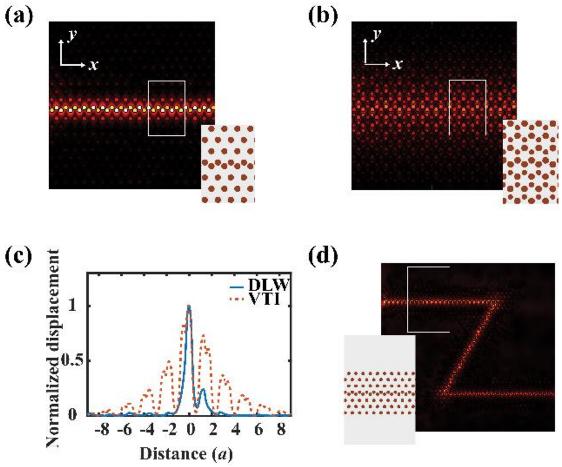

FIG. 6. Confinement of the DLW. (a) The proposed zigzag DLW excited at 76 MHz, with greater confinement. (b) the VTI with $r_B = 0.8r_A$ excited at 76 MHz, shows less confinement. (c) Normalized displacement distribution in y direction (the direction perpendicular to SAW propagation x) for the zigzag DLW compared to that of the VTI. (d) Z-shape zigzag DLW with only 3 rows of pillars on both sides. The inset shows a zoomed-in view.

In addition to its unidirectionality, the DLW shows great confinement of SAW energy. We compare the confinement of the proposed DLW with a VTI. The displacement fields at 76 MHz are shown in **Fig. 6 (a)** and (**b)** for our DLW in contrast to a VTI (**Fig. 2 (b))**, respectively, with the displacement perpendicular to the waveguide plotted in **Fig. 6 (c)**. The DLW shows a much faster decay along the in-plane orthogonal direction y, with 3 dB decay in 0.264a, and 20 dB decay in 0.533a. On the other hand, the displacement for the VTI spreads out 5 times more, with 3 dB decay in 1.324a, and 20 dB decay in 3.140a. The capability of confining SAW in a narrow region allows us to construct a DLW with fewer unit cells in the orthogonal direction. **Fig. 6 (d)** demonstrates that a Z-shape zigzag DLW containing only three unit cells on either side of the interface still guides the SAW as expected.

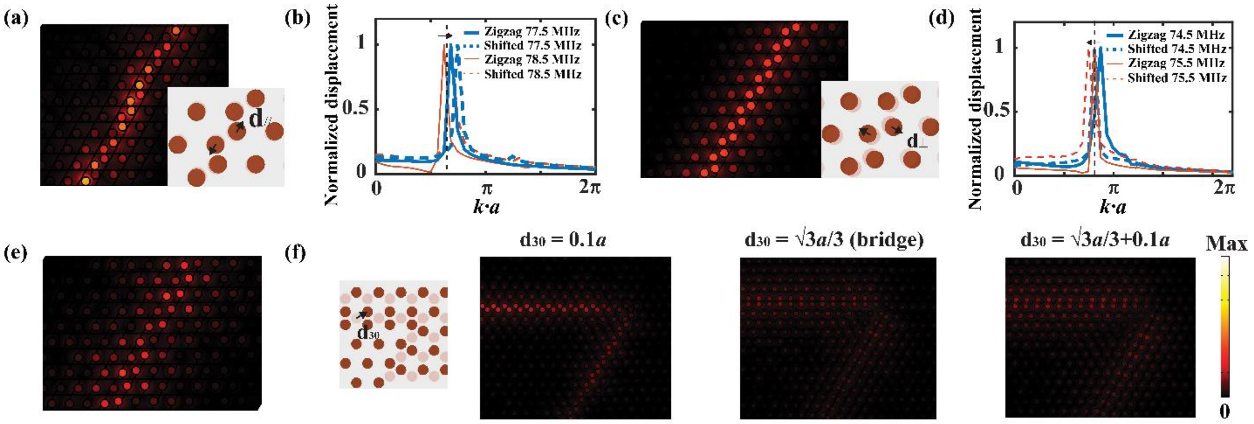

FIG. 7. Robustness of the DLW. (a) A zigzag DLW with a shift $d_{\|} = 0.0425a$ along the waveguide excited. (b) Spatial FFT for u_z along the shifted waveguide in a compared to that of a perfect zigzag DLW at excited 77.5 MHz and 78.5 MHz. When travels at the same wavevector k (same wavelength), the frequency of the interfacial mode is increased from 77.5 MHz to 78 MHz after the $d_{\|}$ shift. (c) A zigzag DLW with a shift $d_{\perp} = 0.05a$ perpendicular to the waveguide. (d) Spatial FFT for u_z along the shifted waveguide in c compared to that of a zigzag DLW at 74.5 MHz and 75.5 MHz. When travels at the same wavevector k (same wavelength), the frequency of the interfacial mode is decreased from 75.5 MHz to 74.5 MHz after the $d_{\perp}$ shift. (e) A zigzag DLW with a shift $d_{\perp} = 0.15a$ perpendicular to the waveguide excited at 74.5 MHz. (f) Bent zigzag DLWs with a shift $d_{30} = 0.1a, \frac{\sqrt{3}}{3}a$ (bridge DLW) and $(\frac{\sqrt{3}}{3} + 0.1)a$ in the direction of 30° towards the waveguide excited at 76MHz, from left to right, respectively.

The waveguides we discussed above are constructed by shifting the pillars to form a perfect zigzag or bridge grain boundary defect line in a triangular lattice. We explored further the configuration of the defect line and how it affects the confinement of the SAW edge states. **Fig. 7(a)** shows a waveguide with the left and right domains of the zigzag interface both shifted in the direction parallel to the interface by $d_{\|} = 0.0425a$, while **Fig. 7(c)** illustrates a waveguide with the left and right domains of the zigzag interface both shifted away from the interface by $d_{\perp} = 0.05a$. It can be observed that the waveguides still support SAW propagation and indicate the robustness of the related edge modes. However, from the spatial FFT for the two cases, as shown in **Fig. 7(b)** and **Fig. 7(d)**, respectively, the edge mode of the same wavelength is shifted to higher or lower frequencies, compared to a perfect zigzag DLW. **Fig. 7(e)** shows the case with a larger perpendicular shifting of $d_{\perp} = 0.15a$, where the SAW is still guided through the interface, but is less confined to the waveguide, compared to a smaller shift in **Fig. 7(c)**. This is because shifting the two domains away from each other will reduce the coupling of the phase vortices at the interface and push the edge modes more towards the lower frequency range, where SAW bulk bands dominate (**Fig. 7(b)**), leading to a less confined interfacial mode. **Fig. 7(f)** shows 120-degree bent DLWs with half of the domain shifted d_{30} in the direction 30° to the zigzag interface. The field plots in **Fig. 7(f)** are for the cases when $d_{30} = 0.1a, \frac{\sqrt{3}}{3}a$ and $(\frac{\sqrt{3}}{3} + 0.1)a$, respectively. Similarly, as the shifting distance d_{30} increases, the SAW also becomes less confined. Note that when $d_{30} = \frac{\sqrt{3}}{3}a$, the waveguide resolves to a perfect bridge interface. As suggested by Fig. **4(b)**, the edge mode of a bridge interface is closer to the SAW bulk band, with slower propagation velocity compared to that of a zigzag interface, resulting in reduced confinement.

D. Experimental observation of the SAW waveguiding

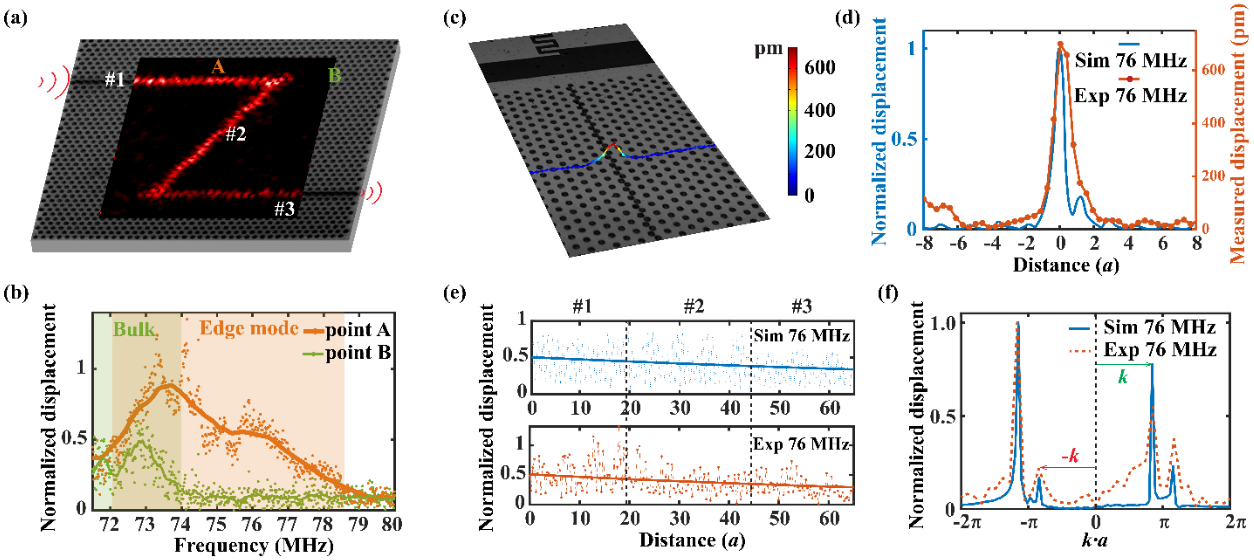

FIG. 8. Experimental demonstration of highly confined unidirectional SAW in a DLW. (a) Measured u_z field for a Z-shaped SAW DLW. The Z shaped waveguide consists of three segments with $26a$ length for each segment, and two 120° sharp turns. The SAW was excited by a broadband IDT with bandwidth in the range of 35 MHz to 90 MHz. The u_z is imaged by the LDV over a 752.15 µm by 612.80 µm rectangular region. The u_z field shown is at 76 MHz. (b) Comparison of u_z for point A on the waveguide and point B away (illustrated in (a)) from the waveguide over the frequency range of 71.5 to 80 MHz, respectively. Measured data is plotted in dots, with the moving average shown as a solid line. (c) Confinement of SAW for the Z-shaped waveguide at 76 MHz. (d) u_z along the direction perpendicular to the propagation direction at 76 MHz for the simulation and the experiment, respectively. (e) (top) Simulated u_z along the waveguide at 76 MHz (dashed line) and fitted exponential decay (solid line). (bottom) Measured u_z along the three segments of the waveguide (illustrated in a) at 76 MHz (dashed line) and fitted exponential decay (solid line). The u_z in (b) and (e) are normalized by the distance between the IDT and the entrance port of the waveguide. (f) Spatial FFT at 76 MHz comparing the simulation with experiment. Displacement is normalized by the largest displacement component from the FFT.

Tightly confined SAW guiding along the proposed DLW, in close accord with the computational simulations of **Figs. 4 and 5**, was experimentally demonstrated in our device, illustrated in **Fig. 8**. The out-of-plane displacement field u_z was measured by a laser Doppler vibrometer (LDV, UHF-120, Polytec). To eliminate possible spurious mode interference from bulk acoustic waves, the back side of the $LiNbO_3$ was roughened. We designed a chirped IDT with a wide bandwidth from 35 MHz to 90 MHz (see **Appendix B**) to excite the SAW and observed unidirectional edge states propagating through a Z-shaped interface with two 120-degree sharp turns. **Fig. 8(a)** depicts the measured out-of-plane SAW displacement field u_z at 76 MHz where a clear surface wave confinement and transport along the DLW is shown. To determine the bandwidth of the edge mode, we compared two points on the device: point **A** on the waveguide and point **B** in the bulk of the triangular crystal, as shown in **Fig. 8(a)**, and their u_z vs. frequency, as shown in **Fig. 8(b)**. Here, the u_z was normalized by the displacement directly in front of the source IDT. It can be clearly seen that away from the waveguide (point **B**) the u_z goes to nearly zero after 74 MHz, which indicates a SAW bandgap for the triangular lattice above 74 MHz. On the other hand, the displacement profile of point A on the waveguide shows a clear bandwidth up to 78.5 MHz, which proves that our edge mode exists in the bulk band of the SAW from 74 MHz to 78.5 MHz. We have also observed guided SAW below the bulk band from 72 MHz to 74 MHz [69], as confirmed through **Fig. 4(b) and Fig. 5(a)**. However, these modes coexist with bulk SAW modes in the background and are less confined. At higher frequencies we note a reduced bandwidth than in simulation, owing to the band edges resulting in flat dispersion, thereby increasing their attenuation and complicating direct observation. To show the confinement of the edge mode in the SAW bandgap, we measured the u_z in the direction perpendicular to the first segment of the Z-shaped waveguide, as shown in **Fig.8(c)**. **Fig. 8(d)** shows that the measured u_z agrees closely with simulation at 76 MHz, and a 3dB decay within $0.509a$ is observed, implying that the mode is highly confined to the interface.

A decay in the displacement amplitude along the waveguide was observed in both the simulation and the measurement [69]. The measured u_z amplitude for the three segments of the Z-shaped waveguide at 76 MHz is shown in the bottom figure of **Fig. 8(e)**, with the simulation result shown in the top figure of **Fig.8(e)**. Assuming a very small reflection at each sharp turn (as justified by the discussion in the next paragraph) and fit the decay of the u_z to be of the form of an exponential decay $Ae^{-\alpha d}$, where A is the amplitude, α is the decay coefficient, and d is the distance the SAW travels along the waveguide, we find α_{sim} =0.00620/a, and α_{exp} =0.00862/a, with the fitted exponential curves plotted in solid lines in **Fig. 8(e)**. This indicates 3dB loss at a distance of ~56a from the entrance port in the simulation, in comparison to ~40a in the measurement.

We quantitively studied the reflection of the SAW and demonstrated there is indeed little reflection at the 120-degree sharp turns. We took the spatial FFT of the u_z along the first segment of the waveguide before the first sharp turn and looked at the wavevectors, as shown in **Fig. 8(f)**. The wavenumber components in **Fig. 8(f)** show a finite value for the negative wavenumber $-k$ within the first BZ ($-\pi$ to π) for both the simulation and the experimental results, indicating there is a small reflection at the 120-degree bends. A higher order component for the same wavevector outside of the first BZ is also observed. We took the average ratio of the displacement component for the k and the $-k$: $r = \frac{u_{z,-k}}{u_{z,k}}$ in the 1st and 2nd BZ (to account for finite edge effects) as the reflection coefficient of the SAW and obtained $r_{sim} = 0.224$ for the simulation, and $r_{exp} = 0.385$ for the measurement. We consider the 3 segments of the Z-shaped waveguide of same acoustic impedance R, so that the SAW energy flux can be expressed as $|u_z|^2/R$. Assuming all the SAW are either reflected or transmitted at the bend, the transmission for the Z-shaped waveguide can be estimated as $t = \sqrt{1-r^2}$, which is t_{sim}= 0.975 for the simulation, and t_{exp}= 0.923, for the measurement. The experimental result indicates that less than 8% of the SAW is reflected in the direction opposite to the incident direction by the two 120-degree bends, proving the directionality of the waveguide. The discrepancies between the simulation and measurement are due to inevitable damping in the sample (e.g., the electroplated copper pillars) and fabrication errors, which are difficult to be precisely simulated.

Ⅲ. CONCLUSION

We have developed a fully integrated on-chip topological SAW unidirectional waveguide, based on defect-line configurations, in a triangular phononic lattice constituted from metallic pillars. Different from spin or valley topological structures, the phononic lattice is trivial with regard to the Berry curvature. Instead, the directionality is maintained by the phase vortex distribution in real space. With half of the total number of pillars needed compared to a VTI ($r_B = 0.8r_A$), the proposed SAW DLW shows better confinement by 5 times in the lateral direction. The confined SAW reduces the number of unit cells needed to construct the waveguide, making it possible to fit many such SAW waveguides on a small chip. Our experiments, in close agreement with simulation results, show successful SAW confinement and routing with small reflection around sharp bends along the propagation path. Our experiments lay the foundation for SAW direction tuning. To enable SAW routing along arbitrary directions, we anticipate the recently found optimal cut of $LiNbO_3$ substrate [84] can be used in place of the industry-standard 127.68^o Y-rotated X-propagating $LiNbO_3$ used in this study. It has been indicated that the proposed DLW is robust in different variations, with the zigzag interface having the widest bandwidth and greatest confinement. Altering the defect boundary shifts the propagation frequency higher or lower and can be potentially used to split frequency components into different directions based on a small difference in the frequency. These results demonstrate the value of this system for further scientific investigations and device development, such as precision removal of cells locally from culture surface [85], multistage cell sorting, high pressure SAW pumping [86] and acoustic streaming [2], would be brought forth through application of our design. By scaling down its dimensions [69], and applying nanoscale detection techniques such as nanowire sensors [97], transmission-mode microwave impedance microscopy (TMIM) [98] and optical pump-probe techniques [99], the proposed waveguide would potentially operate at GHz and work with quantum acoustic platforms.

ACKNOWLEDGEMENTS

The authors thank Nirjhar Sarkar for discussion about the experimental settings. This work was supported by Army Research Office contract W911NF-17-1-0453.

While preparing this manuscript, recent studies [87,88] appeared, which also demonstrate unidirectional SAW devices, though stemming from different (spin/valley-based) origins.

APPENDIX A: SAMPLE PREPARATION

We fabricated chirped interdigital transducers (IDTs) on 500 μm thick, double-side polished 127.68^o Y-rotated X-propagating $LiNbO_3$ (LN, Precision Micro-Optics Inc., Burlington, MA, USA) for surface acoustic wave generation and propagation. Finger widths and finger gaps varying from 26 μm to 11 μm were selected for an operating frequency of 40-90 MHz (from $f = v/\lambda$) to define each IDT, comprised of twenty-five simple finger pairs and linearly distributed gap widths. Standard UV photolithography (using AZ 1512 photoresist and AZ 300MIF developer, MicroChem, Westborough, MA, USA) was used alongside sputter deposition (Denton 18, Denton Vacuum, NJ, USA) and lift-off processes to fabricate the 10 nm Cr / 400 nm Au IDTs and seed layer upon the LN substrate [89,90] . The second layer structure with a thickness of ~15 μm for pillar growth was fabricated via standard UV laser-written photolithography with alignment to the first layer of the IDT structure (using AZ 12XT-20PL-10 photoresist and AZ 300MIF developer, MicroChem, Westborough, MA, USA) (MLA 150, Heidelberg Instruments, Heidelberg, Germany). A dicing saw (Disco Automatic Dicing Saw 3220, Disco, Tokyo, Japan) was used to cut the entire wafer into small size SAW device chips. Then 6.2 μm Cu (copper) was electrochemically deposited on the exposed Au seed layer in an electrolyte environment. The second layer of the photoresist pattern was latter removed by acetone. We observed an accuracy of ± 0.1 um for xy-plane dimensions and $\pm 2\%$ tolerance for the pillar height throughout the sample.

APPENDIX B: EXPERIMENTAL MEASUREMENT

A sinusoidal electric field with input voltage of 0.1 V and sweeping frequency from 35-95 MHz was applied to the IDT to excite a broadband input signal into the entrance port of the SAW waveguide using a signal generator (WF1967 multifunction generator, NF Corporation, Yokohama, Japan) and amplifier (ZHL-1-2W-S+, Mini-Circuits, Brooklyn, NY, USA). The actual voltage, current, and power across the device were measured using a digital storage oscilloscope (InfiniiVision 2000 X-Series, Keysight Technologies, Santa Rosa, CA). The source IDT is of the aperture of $1.44a$ (overlapping width) and is $5.2a$ away from the entrance port of the waveguide. To eliminate reflections at the boundaries of the device, a SAW absorber (Dragon Skin 10 Medium, Smooth-On, Inc., Macungie, PA, USA) is placed around the edge of the sample. The backside of the $LiNbO_3$ wafer is roughened to absorb possible reflection of the bulk acoustic wave at the bottom of the wafer. The out-of-plane displacement magnitude and phase fields are captured by a laser Doppler vibrometer (LDV, UHF–120, Polytec, Waldbronn, Germany). The data presented is the average after 10 measurements from the LDV.

APPENDIX C: NUMBERICAL SIMULATION

The eigen-mode and the driven-mode simulations were implemented using the commercial software COMSOL Multiphysics with the Acoustic (Acoustic-Solid Interaction) and Electrostatics modules, based on the finite element method. Floquet periodic boundaries were assigned for unit cell and supercell band diagram calculations, while the low-reflection boundary was imposed on the outer boundaries for the frequency domain driven-mode studies. A fixed boundary is always applied at the bottom of the $LiNbO_3$ substrate. On the band diagrams for the unit cells, the SAW modes can be distinguished under the sound cone, which is formed by the slowest bulk mode dispersion. In the driven mode simulation, we excite the SAW by applying a sinusoidal edge load or a point load on the substrate. For the material properties, we used the z-cut $LiNbO_3$ parameters with a rotated coordinate system to get the properties for the 127.68^{o}-degree Y/X-cut $LiNbO_3$ wafers. The elastic parameters of the Cu pillars used in the calculations are density $\rho_{\mathrm{Cu}} = 8960\,\mathrm{kg\,m^{-3}}$, Young's modulus $E_{\mathrm{Ni}} = 70$ GPa and Poisson's ratio ν_{Cu}=0.34. Note that the Young's modulus is smaller than the conventional Young's modulus for Cu, due to our specific plating process. It was also found in the literature that Young's modulus can be sensitive to plating conditions [91].

For the Berry curvature calculation [72], the complex out-of-plane displacement with magnitude and phase information in the real-space domain is exported from COMSOL simulations for each wavevector for the integration.

[1] J. Friend and L. Y. Yeo, *Microscale Acoustofluidics: Microfluidics Driven via Acoustics and Ultrasonics*, Rev. Mod. Phys. **83**, 647 (2011).

[2] N. Zhang, A. Horesh, O. Manor, and J. Friend, *Powerful Acoustogeometric Streaming from Dynamic Geometric Nonlinearity*, Phys. Rev. Lett. **126**, 164502 (2021).

[3] N. Zhang, A. Horesh, and J. Friend, *Manipulation and Mixing of 200 Femtoliter Droplets in Nanofluidic Channels Using MHz-Order Surface Acoustic Waves*, Adv. Sci. **8**, 2100408 (2021).

[4] W. Connacher, J. Orosco, and J. Friend, *Droplet Ejection at Controlled Angles via Acoustofluidic Jetting*, Phys. Rev. Lett. **125**, 184504 (2020).

[5] R. H. Liu, J. Yang, M. Z. Pindera, M. Athavale, and P. Grodzinski, *Bubble-Induced Acoustic Micromixing*, Lab Chip **2**, 151 (2002).

[6] Y. Zhang, C. Devendran, C. Lupton, A. De Marco, and A. Neild, *Versatile Platform for Performing Protocols on a Chip Utilizing Surface Acoustic Wave (SAW) Driven Mixing*, Lab Chip **19**, 262 (2019).

[7] Y. Gu, C. Chen, Z. Mao, H. Bachman, R. Becker, J. Rufo, Z. Wang, P. Zhang, J. Mai, S. Yang, J. Zhang, S. Zhao, Y. Ouyang, D. T. W. Wong, Y. Sadovsky, and T. J. Huang, *Acoustofluidic Centrifuge for Nanoparticle Enrichment and Separation*, Sci. Adv. **7**, eabc0467 (2021).

[8] A. Ozcelik, J. Rufo, F. Guo, Y. Gu, P. Li, J. Lata, and T. J. Huang, *Acoustic Tweezers for the Life Sciences*, Nat. Methods **15**, 1021 (2018).

[9] B. Kang, J. Shin, H. J. Park, C. Rhyou, D. Kang, S. J. Lee, Y. sup Yoon, S. W. Cho, and H. Lee, *High-Resolution Acoustophoretic 3D Cell Patterning to Construct Functional Collateral Cylindroids for Ischemia Therapy*, Nat. Commun. **9**, 5402 (2018).

[10] J. P. Lata, F. Guo, J. Guo, P. H. Huang, J. Yang, and T. J. Huang, *Surface Acoustic Waves Grant Superior Spatial Control of Cells Embedded in Hydrogel Fibers*, Adv. Mater. **28**, 8632 (2016).

[11] K. J. Satzinger, Y. P. Zhong, H.-S. Chang, G. A. Peairs, A. Bienfait, M.-H. Chou, A. Y. Cleland, C. R. Conner, É. Dumur, J. Grebel, I. Gutierrez, B. H. November, R. G. Povey, S. J. Whiteley, D. D. Awschalom, D. I. Schuster, and A. N. Cleland, *Quantum Control of Surface Acoustic-Wave Phonons*, Nature **563**, 661 (2018).

[12] Y. Chu, P. Kharel, W. H. Renninger, L. D. Burkhart, L. Frunzio, P. T. Rakich, and R. J. Schoelkopf, *Quantum Acoustics with Superconducting Qubits*, Science **358**, 199 (2017).

[13] R. Manenti, M. J. Peterer, A. Nersisyan, E. B. Magnusson, A. Patterson, and P. J. Leek, *Surface Acoustic Wave Resonators in the Quantum Regime*, Phys. Rev. B **93**, 041411 (2016).

[14] C. H. W. Barnes, J. M. Shilton, and A. M. Robinson, *Quantum Computation Using Electrons Trapped by Surface Acoustic Waves*, Phys. Rev. B **62**, 8410 (2000).

[15] S. Hermelin, S. Takada, M. Yamamoto, S. Tarucha, A. D. Wieck, L. Saminadayar, C. Bäuerle, and T. Meunier, *Electrons Surfing on a Sound Wave as a Platform for Quantum Optics with Flying Electrons*, Nature **477**, 435 (2011).

[16] R. P. G. McNeil, M. Kataoka, C. J. B. Ford, C. H. W. Barnes, D. Anderson, G. A. C. Jones, I. Farrer, and D. A. Ritchie, *On-Demand Single-Electron Transfer between Distant Quantum Dots*, Nature **477**, 439 (2011).

[17] J. MEI and J. FRIEND, *A Review: Controlling the Propagation of Surface Acoustic Waves via Waveguides for Potential Use in Acoustofluidics*, Mech. Eng. Rev. **7**, 19 (2020).

[18] A. J. Slobodnik and E. D. Conway, *The Effect of Beam Steering on the Design of Microwave Acoustic Surface Wave Devices*, in *G-MTT 1970 International Microwave Symposium*, Vol. 13 (IEEE, 1970), pp. 314–318.

[19] A. Hagelauer, G. Fattinger, C. C. W. Ruppel, M. Ueda, K. Hashimoto, and A. Tag, *Microwave Acoustic Wave Devices: Recent Advances on Architectures, Modeling, Materials, and Packaging*, IEEE Trans. Microw. Theory Tech. **66**, 4548 (2018).

[20] P. Delsing, A. N. Cleland, M. J. A. Schuetz, J. Knörzer, G. Giedke, J. I. Cirac, K. Srinivasan, M. Wu, K. C. Balram, C. Bäuerle, T. Meunier, C. J. B. Ford, P. V. Santos, E. Cerda-Méndez, H. Wang, H. J. Krenner, E. D. S. Nysten, M. Weiß, G. R. Nash, L. Thevenard, C. Gourdon, P. Rovillain, M. Marangolo, J.-Y. Duquesne, G. Fischerauer, W. Ruile, A. Reiner, B. Paschke, D. Denysenko, D. Volkmer, A. Wixforth, H. Bruus, M. Wiklund, J. Reboud, J. M. Cooper, Y. Fu, M. S. Brugger, F.

Rehfeldt, and C. Westerhausen, *The 2019 Surface Acoustic Waves Roadmap*, J. Phys. D. Appl. Phys. **52**, 353001 (2019).

[21] T. Nomura, X. X. Zhang, S. Zherlitsyn, J. Wosnitza, Y. Tokura, N. Nagaosa, and S. Seki, *Phonon Magnetochiral Effect*, Phys. Rev. Lett. **122**, 145901 (2019).

[22] R. Sasaki, Y. Nii, Y. Iguchi, and Y. Onose, *Nonreciprocal Propagation of Surface Acoustic Wave in Ni/LiNbO3*, Phys. Rev. B **95**, 020407 (2017).

[23] R. Verba, I. Lisenkov, I. Krivorotov, V. Tiberkevich, and A. Slavin, *Nonreciprocal Surface Acoustic Waves in Multilayers with Magnetoelastic and Interfacial Dzyaloshinskii-Moriya Interactions*, Phys. Rev. Appl. **9**, 64014 (2018).

[24] M. Küß, M. Heigl, L. Flacke, A. Hörner, M. Weiler, A. Wixforth, and M. Albrecht, *Nonreciprocal Magnetoacoustic Waves in Dipolar-Coupled Ferromagnetic Bilayers*, Phys. Rev. Appl. **15**, 034060 (2021).

[25] P. J. Shah, D. A. Bas, I. Lisenkov, A. Matyushov, N. X. Sun, and M. R. Page, *Giant Nonreciprocity of Surface Acoustic Waves Enabled by the Magnetoelastic Interaction*, Sci. Adv. **6**, eabc5648 (2020).

[26] M. Xu, K. Yamamoto, J. Puebla, K. Baumgaertl, B. Rana, K. Miura, H. Takahashi, D. Grundler, S. Maekawa, and Y. Otani, *Nonreciprocal Surface Acoustic Wave Propagation via Magneto-Rotation Coupling*, Sci. Adv. **6**, eabb1724 (2020).

[27] B. Liang, B. Yuan, and J. C. Cheng, *Acoustic Diode: Rectification of Acoustic Energy Flux in One-Dimensional Systems*, Phys. Rev. Lett. **103**, 104301 (2009).

[28] B. Liang, X. S. Guo, J. Tu, D. Zhang, and J. C. Cheng, *An Acoustic Rectifier*, Nat. Mater. **9**, 989 (2010).

[29] N. Boechler, G. Theocharis, and C. Daraio, *Bifurcation-Based Acoustic Switching and Rectification*, Nat. Mater. **10**, 665 (2011).

[30] L. Shao, W. Mao, S. Maity, N. Sinclair, Y. Hu, L. Yang, and M. Lončar, *Non-Reciprocal Transmission of Microwave Acoustic Waves in Nonlinear Parity–Time Symmetric Resonators*, Nat. Electron. **3**, 267 (2020).

[31] M. Z. Hasan and C. L. Kane, *Colloquium : Topological Insulators*, Rev. Mod. Phys. **82**, 3045 (2010).

[32] X.-L. Qi and S.-C. Zhang, *Topological Insulators and Superconductors*, Rev. Mod. Phys. **83**, 1057 (2011).

[33] L. Lu, J. D. Joannopoulos, and M. Soljačić, *Topological Photonics*, Nat. Photonics **8**, 821 (2014).

[34] T. Ozawa, H. M. Price, A. Amo, N. Goldman, M. Hafezi, L. Lu, M. C. Rechtsman, D. Schuster, J. Simon, O. Zilberberg, and I. Carusotto, *Topological Photonics*, Rev. Mod. Phys. **91**, 015006 (2019).

[35] F. D. M. Haldane and S. Raghu, *Possible Realization of Directional Optical Waveguides in Photonic Crystals with Broken Time-Reversal Symmetry*, Phys. Rev. Lett. **100**, 013904 (2008).

[36] S. Raghu and F. D. M. Haldane, *Analogs of Quantum-Hall-Effect Edge States in Photonic Crystals*, Phys. Rev. A **78**, 033834 (2008).

[37] Z. Wang, Y. D. Chong, J. D. Joannopoulos, and M. Soljačić, *Reflection-Free One-Way Edge Modes in a Gyromagnetic Photonic Crystal*, Phys. Rev. Lett. **100**, 013905 (2008).

[38] B. Bahari, L. Hsu, S. H. Pan, D. Preece, A. Ndao, A. El Amili, Y. Fainman, and B. Kanté, *Photonic Quantum Hall Effect and Multiplexed Light Sources of Large Orbital Angular Momenta*, Nat. Phys. **17**, 700 (2021).

[39] H. Chorsi, B. Cheng, B. Zhao, J. Toudert, V. Asadchy, O. F. Shoron, S. Fan, and R. Matsunaga, *Topological Materials for Functional Optoelectronic Devices*, Adv. Funct. Mater. **32**, 2110655 (2022).

[40] Z. Xu, X. Kong, R. J. Davis, D. Bisharat, Y. Zhou, X. Yin, and D. F. Sievenpiper, *Topological Valley Transport under Long-Range Deformations*, Phys. Rev. Res. **2**, 013209 (2020).

[41] G. Ma, M. Xiao, and C. T. Chan, *Topological Phases in Acoustic and Mechanical Systems*, Nat. Rev. Phys. **1**, 281 (2019).

[42] S. D. Huber, *Topological Mechanics*, Nat. Phys. **12**, 621 (2016).

[43] Z. Yang, F. Gao, X. Shi, X. Lin, Z. Gao, Y. Chong, and B. Zhang, *Topological Acoustics*, Phys. Rev. Lett. **114**, 114301 (2015).

[44] Y. Ding, Y. Peng, Y. Zhu, X. Fan, J. Yang, B. Liang, X. Zhu, X. Wan, and J. Cheng, *Experimental Demonstration of Acoustic Chern Insulators*, Phys. Rev. Lett. **122**, 014302 (2019).

[45] P. Wang, L. Lu, and K. Bertoldi, *Topological Phononic Crystals with One-Way Elastic Edge Waves*, Phys. Rev. Lett. **115**, 104302 (2015).

[46] L. M. Nash, D. Kleckner, A. Read, V. Vitelli, A. M. Turner, and W. T. M. Irvine, *Topological Mechanics of Gyroscopic Metamaterials*, Proc. Natl. Acad. Sci. **112**, 14495 (2015).

[47] R. Fleury, D. L. Sounas, C. F. Sieck, M. R. Haberman, and A. Alu, *Sound Isolation and Giant Linear Nonreciprocity in a Compact Acoustic Circulator*, Science **343**, 516 (2014).

[48] A. B. Khanikaev, R. Fleury, S. H. Mousavi, and A. Alù, *Topologically Robust Sound Propagation in an Angular-Momentum-Biased Graphene-like Resonator Lattice*, Nat. Commun. **6**, 8260 (2015).

[49] Y. Liu, X. Chen, and Y. Xu, *Topological Phononics: From Fundamental Models to Real Materials*, Adv. Funct. Mater. **30**, 1904784(2020).

[50] B. A. Bernevig and S.-C. Zhang, *Quantum Spin Hall Effect*, Phys. Rev. Lett. **95**, 016801 (2005).

[51] C. L. Kane and E. J. Mele, *Quantum Spin Hall Effect in Graphene*, Phys. Rev. Lett. **95**, 226801 (2005).

[52] M. Konig, S. Wiedmann, C. Brune, A. Roth, H. Buhmann, L. W. Molenkamp, X.-L. Qi, and S.-C. Zhang, *Quantum Spin Hall Insulator State in HgTe Quantum Wells*, Science **318**, 766 (2007).

[53] C. L. Kane and E. J. Mele, *Z2 Topological Order and the Quantum Spin Hall Effect*, Phys. Rev. Lett. **95**, 146802 (2005).

[54] L.-H. Wu and X. Hu, *Scheme for Achieving a Topological Photonic Crystal by Using Dielectric Material*, Phys. Rev. Lett. **114**, 223901 (2015).

[55] Y. Zhou, P. R. Bandaru, and D. F. Sievenpiper, *Quantum-Spin-Hall Topological Insulator in a Spring-Mass System*, New J. Phys. **20**, 123011 (2018).

[56] C. He, X. Ni, H. Ge, X.-C. Sun, Y.-B. Chen, M.-H. Lu, X.-P. Liu, and Y.-F. Chen, *Acoustic Topological Insulator and Robust One-Way Sound Transport*, Nat. Phys. **12**, 1124 (2016).

[57] J. P. Xia, D. Jia, H. X. Sun, S. Q. Yuan, Y. Ge, Q. R. Si, and X. J. Liu, *Programmable Coding*

Acoustic Topological Insulator, Adv. Mater. **30**, 1805002 (2018).

[58] T. Ma, A. B. Khanikaev, S. H. Mousavi, and G. Shvets, *Guiding Electromagnetic Waves around Sharp Corners: Topologically Protected Photonic Transport in Metawaveguides*, Phys. Rev. Lett. **114**, 127401 (2015).

[59] S. H. Mousavi, A. B. Khanikaev, and Z. Wang, *Topologically Protected Elastic Waves in Phononic Metamaterials*, Nat. Commun. **6**, 8682 (2015).

[60] D. J. Bisharat and D. F. Sievenpiper, *Electromagnetic-Dual Metasurfaces for Topological States along a 1D Interface*, Laser Photonics Rev. **13**, 1900126 (2019).

[61] Z. Tian, C. Shen, J. Li, E. Reit, H. Bachman, J. E. S. Socolar, S. A. Cummer, and T. Jun Huang, *Dispersion Tuning and Route Reconfiguration of Acoustic Waves in Valley Topological Phononic Crystals*, Nat. Commun. **11**, 762 (2020).

[62] Z. Zhang, Y. Tian, Y. Wang, S. Gao, Y. Cheng, X. Liu, and J. Christensen, *Directional Acoustic Antennas Based on Valley-Hall Topological Insulators*, Adv. Mater. **30**, 1803229 (2018).

[63] M. Yan, J. Lu, F. Li, W. Deng, X. Huang, J. Ma, and Z. Liu, *On-Chip Valley Topological Materials for Elastic Wave Manipulation*, Nat. Mater. **17**, 993 (2018).

[64] J. Cha, K. W. Kim, and C. Daraio, *Experimental Realization of On-Chip Topological Nanoelectromechanical Metamaterials*, Nature **564**, 229 (2018).

[65] J. Ma, X. Xi, and X. Sun, *Experimental Demonstration of Dual-Band Nano-Electromechanical Valley-Hall Topological Metamaterials*, Adv. Mater. **33**, 2006521 (2021).

[66] S.-Y. Yu, X.-C. Sun, X. Ni, Q. Wang, X.-J. Yan, C. He, X.-P. Liu, L. Feng, M.-H. Lu, and Y.-F. Chen, *Surface Phononic Graphene*, Nat. Mater. **15**, 1243 (2016).

[67] Z. Wang, F.-K. Liu, S.-Y. Yu, S.-L. Yan, M.-H. Lu, Y. Jing, and Y.-F. Chen, *Guiding Robust Valley-Dependent Edge States by Surface Acoustic Waves*, J. Appl. Phys. **125**, 044502 (2019).

[68] D. J. Bisharat and D. F. Sievenpiper, *Valley polarized edge states beyond inversion symmetry breaking*, arXiv:2301.07349 (2023).

[69] See Supplemental Material at [URL will be inserted by publisher] for theoretical details of the topological characterization of the proposed structure, and some additional simulation and experimental results.

[70] J. K. Yang, Y. Hwang, and S. S. Oh, *Evolution of Topological Edge Modes from Honeycomb Photonic Crystals to Triangular-Lattice Photonic Crystals*, Phys. Rev. Res. **3**, L022025 (2021).

[71] D. Xiao, W. Yao, and Q. Niu, *Valley-Contrasting Physics in Graphene: Magnetic Moment and Topological Transport*, Phys. Rev. Lett. **99**, 236809 (2007).

[72] X.-T. He, E.-T. Liang, J.-J. Yuan, H.-Y. Qiu, X.-D. Chen, F.-L. Zhao, and J.-W. Dong, *A Silicon-on-Insulator Slab for Topological Valley Transport*, Nat. Commun. **10**, 872 (2019).

[73] D. J. Bisharat, R. J. Davis, Y. Zhou, P. R. Bandaru, D. F. Sievenpiper, and C. Caloz, *Photonic Topological Insulators : A Beginner's Introduction [Electromagnetic Perspectives],* IEEE Antennas Propag. Mag. **63**, 112 (2021).

[74] F. Liu and K. Wakabayashi, *Novel Topological Phase with a Zero Berry Curvature*, Phys. Rev. Lett. **118**, 076803 (2017).

[75] F. D. M. Haldane, *Berry Curvature on the Fermi Surface: Anomalous Hall Effect as a Topological Fermi-Liquid Property*, Phys. Rev. Lett. **93**, 206602 (2004).

[76] H.-M. Guo and M. Franz, *Topological Insulator on the Kagome Lattice*, Phys. Rev. B **80**, 113102 (2009).

[77] H. Xue, Y. Yang, F. Gao, Y. Chong, and B. Zhang, *Acoustic Higher-Order Topological Insulator on a Kagome Lattice*, Nat. Mater. **18**, 108 (2019).

[78] M. Li, D. Zhirihin, M. Gorlach, X. Ni, D. Filonov, A. Slobozhanyuk, A. Alù, and A. B. Khanikaev, *Higher-Order Topological States in Photonic Kagome Crystals with Long-Range Interactions*, Nat. Photonics **14**, 89 (2020).

[79] H.-X. Wang, L. Liang, B. Jiang, J. Hu, X. Lu, and J.-H. Jiang, *Higher-Order Topological Phases in Tunable C 3 Symmetric Photonic Crystals* , Photonics Res. **9**, 1854 (2021).

[80] W. A. Benalcazar, T. Li, and T. L. Hughes, *Quantization of Fractional Corner Charge in C_n -Symmetric Higher-Order Topological Crystalline Insulators*, Phys. Rev. B **99**, 245151 (2019).

[81] T. Li, P. Zhu, W. A. Benalcazar, and T. L. Hughes, *Fractional Disclination Charge in Two-Dimensional C_n -Symmetric Topological Crystalline Insulators*, Phys. Rev. B **101**, 115115 (2020).

[82] Y. Liu, S. Leung, F.-F. Li, Z.-K. Lin, X. Tao, Y. Poo, and J.-H. Jiang, *Bulk–Disclination Correspondence in Topological Crystalline Insulators*, Nature **589**, 381 (2021).

[83] R. J. Davis, Y. Zhou, D. J. Bisharat, P. R. Bandaru, and D. F. Sievenpiper, *Topologically Protected Edge States in Triangular Lattices*, Phys. Rev. B **106**, 165403 (2022).

[84] N. Zhang, J. Mei, T. Gopesh, and J. Friend, *Optimized, Omnidirectional Surface Acoustic Wave Source: 152° Y-Rotated Cut of Lithium Niobate for Acoustofluidics*, IEEE Trans. Ultrason. Ferroelectr. Freq. Control **67**, 2176 (2020).

[85] T. Inui, J. Mei, C. Imashiro, Y. Kurashina, J. Friend, and K. Takemura, *Focused Surface Acoustic Wave Locally Removes Cells from Culture Surface*, Lab Chip **21**, 1299 (2021).

[86] S. M. Langelier, L. Y. Yeo, and J. Friend, *UV Epoxy Bonding for Enhanced SAW Transmission and Microscale Acoustofluidic Integration*, Lab Chip **12**, 2970 (2012).

[87] Z. D. Zhang, S. Y. Yu, H. Ge, J. Q. Wang, H. F. Wang, K. F. Liu, T. Wu, C. He, M. H. Lu, and Y. F. Chen, *Topological Surface Acoustic Waves*, Phys. Rev. Appl. **16**, 044008 (2021).

[88] J. Q. Wang, Z. D. Zhang, S. Y. Yu, H. Ge, K. F. Liu, T. Wu, X. C. Sun, L. Liu, H. Y. Chen, C. He, M. H. Lu, and Y. F. Chen, *Extended Topological Valley-Locked Surface Acoustic Waves*, Nat. Commun. **13**, 1324 (2022).

[89] J. Mei, N. Zhang, and J. Friend, *Fabrication of Surface Acoustic Wave Devices on Lithium Niobate*, J. Vis. Exp. **160**, e61013 (2020).

[90] W. Connacher, N. Zhang, A. Huang, J. Mei, S. Zhang, T. Gopesh, and J. Friend, *Micro/Nano Acoustofluidics: Materials, Phenomena, Design, Devices, and Applications*, Lab Chip **18**, 1952 (2018).

[91] J. LUO, *Young's Modulus of Electroplated Ni Thin Film for MEMS Applications*, Mater. Lett. **58**, 2306 (2004).

[92] A. Khelif, P. A. Deymier, B. Djafari-Rouhani, J. O. Vasseur, and L. Dobrzynski, *Two-Dimensional Phononic Crystal with Tunable Narrow Pass Band: Application to a Waveguide with Selective*

Frequency, J. Appl. Phys. **94**, 1308 (2003).

[93] A. Khelif, A. Choujaa, S. Benchabane, B. Djafari-Rouhani, and V. Laude, *Guiding and Bending of Acoustic Waves in Highly Confined Phononic Crystal Waveguides*, Appl. Phys. Lett. **84**, 4400 (2004).

[94] M. Wilm, A. Khelif, S. Ballandras, V. Laude, and B. Djafari-Rouhani, *Out-of-Plane Propagation of Elastic Waves in Two-Dimensional Phononic Band-Gap Materials*, Phys. Rev. E **67**, 065602(R) (2003).

[95] A. Khelif, B. Djafari-Rouhani, O. Vasseur, and A. Deymier, *Transmission and Dispersion Relations of Perfect and Defect-Containing Waveguide Structures in Phononic Band Gap Materials*, Phys. Rev. B **68**, 024302 (2003).

[96] A. Khelif, A. Choujaa, B. Djafari-Rouhani, M. Wilm, S. Ballandras, and V. Laude, *Trapping and Guiding of Acoustic Waves by Defect Modes in a Full-Band-Gap Ultrasonic Crystal*, Phys. Rev. B **68**, 214201 (2003).

[97] M. M. Sonner, F. Khosravi, L. Janker, D. Rudolph, G. Koblmüller, Z. Jacob, and H. J. Krenner, *Ultrafast Electron Cycloids Driven by the Transverse Spin of a Surface Acoustic Wave*, Sci. Adv. **7**, eabf7414 (2021).

[98] D. Lee, Q. Liu, L. Zheng, X. Ma, H. Li, M. Li, and K. Lai, *Direct Visualization of Gigahertz Acoustic Wave Propagation in Suspended Phononic Circuits*, Phys. Rev. Appl. **16**, 304047 (2021).

[99] D. Li and D. G. Cahill, *Attenuation of 7 GHz Surface Acoustic Waves on Silicon*, Phys. Rev. B **94**, 104306 (2016).

[100] W. Hergert, and R. M. Geilhufe, *Group Theory in Solid State Physics and Photonics: Problem Solving with Mathematica* (Wiley-VCH, New York, 2018).